

Plastically Bendable Organic Crystals for Monolithic and Hybrid Micro-Optical Circuits

Jada Ravi, Torvid Feiler, Amit Mondal, Adam A. L. Michalchuk, C. Malla Reddy,*
 Biswajit Bhattacharya,* Franziska Emmerling,* and Rajadurai Chandrasekar*

Fluorescent plastically bendable crystals are a promising alternative to silicon-based materials for fabricating photonic integrated circuits, owing to their optical attributes and mechanical compliance. Mechanically bendable plastic organic crystals are rare. Their formation requires anisotropic intermolecular interactions and slip planes in the crystal lattice. This work presents three fluorescent plastically bendable crystalline materials namely, 2-((E)-(6-methylpyridin-2-ylimino)methyl)-4-chlorophenol (SB1), 2-((E)-(6-methylpyridin-2-ylimino)methyl)-4-bromophenol (SB2), and 2-((E)-(6-Bromopyridin-2-ylimino)methyl)-4-bromophenol (SB3) molecules. The crystal plasticity in response to mechanical stress facilitates the fabrication of various monolithic and hybrid (with a tip-to-tip coupling) photonic circuits using mechanical micromanipulation with an atomic force microscope cantilever tip. These plastically bendable crystals act as active (self-guiding of fluorescence) and passive waveguides both in straight and extremely bent (U-, J-, and O-shaped) geometries. These microcircuits use active and passive waveguiding principles and reabsorbance and energy-transfer mechanisms for their operation, allowing input-selective and direction-specific signal transduction.


1. Introduction

Organic photonic integrated circuits (OPICs) are emerging as a promising alternative to electronic circuits for light-based

J. Ravi, R. Chandrasekar
 Advanced Organic Photonic Materials and Technology Laboratory
 School of Chemistry and Centre for Nanotechnology
 University of Hyderabad
 Gachibowli, Hyderabad 500046, India
 E-mail: r.chandrasekar@uohyd.ac.in

T. Feiler, A. A. L. Michalchuk, B. Bhattacharya, F. Emmerling
 BAM Federal Institute for Materials Research and Testing
 Richard-Willstätter-Str. 11 12489 Berlin, Germany
 E-mail: biswajit.bhattacharya@bam.de; franziska.emmerling@bam.de

A. Mondal, C. M. Reddy
 Department of Chemical Sciences
 Indian Institute of Science Education and Research (IISER) Kolkata
 Mohanpur, Nadia, West Bengal 741246, India
 E-mail: cmreddy@iiserkol.ac.in

 The ORCID identification number(s) for the author(s) of this article can be found under <https://doi.org/10.1002/adom.202201518>.

© 2022 The Authors. Advanced Optical Materials published by Wiley-VCH GmbH. This is an open access article under the terms of the Creative Commons Attribution License, which permits use, distribution and reproduction in any medium, provided the original work is properly cited.

DOI: 10.1002/adom.202201518

device technologies.^[1–4] Photonic integrated circuits (PICs) have the advantage of ultra-fast information transfer with a simultaneous higher information-carrying capability.^[5–8] Optical waveguides are one of the central components for high-speed data transfer in PICs.^[5] Most PICs are made of silicon-based waveguides on silica substrate because of the former's high refractive index ($n = 3.47$), providing better light confinement and low optical loss at extreme bends.^[3,4] Waveguides are divided into active^[9] and passive^[10] types depending on the optical transmission type. Both types of waveguides are essential for PIC operation. Silicon-based waveguides are passive and require complex manufacturing procedures using electron beam lithography.^[6] Moreover, silicon-based materials are rigid (Young's modulus of ≈ 150 GPa, and Poisson's ratio of ≈ 0.17) and non-reconfigurable.

New flexible photonic materials are needed to construct next-generation flexible circuit technologies.^[1,2] Organic crystals are a potential choice as photonic materials because they possess relatively high $n \approx 1.7$ compared to silica, room temperature exciton-polariton formation,^[7] tunable optical bandwidth,^[8] optical nonlinearity,^[11] chirality,^[12] solution processability, and mechanical compliance.^[11–15] Takazawa et al. demonstrated flexible thiocyanine nanofibers as active waveguides.^[11] Chandrasekar et al. reported the passive type of light transduction in 180° bent waveguide using a flexible organic microcrystal.^[12] To fabricate organic PICs, waveguides,^[16,17] add-drop filters,^[18,19] resonators (ring, disk, microsphere),^[11,12,20,21] modulators,^[16] directional couplers,^[22] and lasers,^[23] are necessary components. Desiraju and Reddy provided the molecular structure basis for mechanical plasticity and elasticity in organic crystals.^[13,14] Conventionally, most bending tests on flexible crystals were performed using a three-point bending technique with a pair of forceps and a metal needle with oil as a lubricant.^[11,13–15,24] Implementing flexible optical crystals in PICs for miniaturized technological applications requires suitable micron-sized crystals and innovative processing strategies.^[1,2] It has been recently established that, depending on the crystal thickness, flexible microcrystals show pseudo-plasticity during mechanical manipulation without any lubricant.^[17,19,22,25] It is expected that this pseudo-plasticity is due to strong adhesive interaction with the silica surface compared to the shape regaining energy.

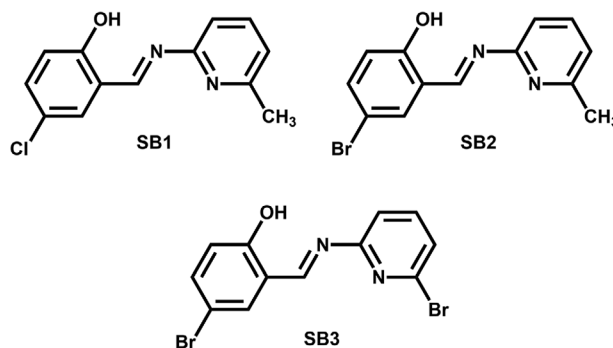
Mechanophotonics – a technique to mechanically manipulate microcrystal waveguides using an atomic force microscope (AFM) cantilever tip has been demonstrated.^[1–3] Various micromechanical manipulation operations, including bending, lifting, cutting, slicing, transferring, and integrating crystals, have been developed for circuit construction.^[1] With the high accuracy of the micromanipulation process, desirable light pathways through crystals can be realized. As a result of this unique approach, oil-free, proof-of-principle monolithic, and hetero PICs have been made using elastic micro-sized crystals on silica substrates.^[1,19,22,25] For example, a combination of ring resonators and optical waveguides has been realized to route the light in a clockwise and anticlockwise directions in a circuit.^[19,25] Here, the unique arrangement of components and signal transduction via active, passive, reabsorbance, and energy-transfer mechanisms allowed input-selective and direction-specific signal modification. PICs, constructed with plastic and elastic bendable crystals, have been used to route the light in different directions.^[25a] However, an entirely plastically bendable crystal-based photonic circuit has not yet been made. Unlike elastic crystals, the inherent mechanical plasticity of the crystals facilitates their deployment on surfaces to obtain desirable 2D PIC geometries without relying on pseudo-plasticity.

The PIC materials must combine mechanical flexibility and optical properties to realize next-generation technologies. Using molecules with a Schiff base backbone with π -conjugation is proven effective in designing such materials.^[17e,24c,d,25b] Besides mechanical compliance, such molecules are also well-known for having high photoluminescence.^[26] Mechanical compliance can be introduced into the crystal packing by incorporating methyl and bromine as side groups on the Schiff base backbone.^[13d] We here report the synthesis of three molecules, namely 2-((*E*)-(6-methylpyridin-2-ylimino)methyl)-4-chlorophenol (SB1), 2-((*E*)-(6-methylpyridin-2-ylimino)methyl)-4-bromophenol (SB2), and 2-((*E*)-(6-bromopyridin-2-ylimino)methyl)-4-bromophenol (SB3) via mechanochemistry. The unique anisotropic molecular packing with slip planes supports the mechanical plasticity of SB1, SB2, and SB3 crystals. The micro-sized crystals act as active optical waveguides transmitting yellow and green fluorescence efficiently. The plasticity of crystals facilitates the construction of monolithic and hybrid (tip-to-tip coupled) circuits using the mechanophotonics approach. The PICs operate using active, passive, reabsorbance, and energy-transfer mechanisms allowing input-selective and direction-specific signal transmissions.^[1,2]

2. Results and Discussion

2.1. Synthesis and Crystal Structure

Three salicylaldehydederived Schiff bases, SB1, SB2, and SB3 (Scheme 1), were synthesized by liquid-assisted grinding of a stoichiometric mixture of the corresponding amine and aldehyde (Section S1.2, Supporting Information). Single crystals of all three compounds were grown in glass tubes using a solvent/anti-solvent layering technique. The ground powder was dissolved in dichloromethane, followed by n-hexane layering. Orange block-shaped crystals appeared at the phase boundary after a week.



Scheme 1. Molecular structures of SB1–SB3.

X-ray single-crystal structure determination revealed that SB1 crystallizes in the monoclinic space group $P2_1/c$ with one molecule in the asymmetric unit in a slightly twisted planar conformation. The dihedral angle between the pyridyl and phenolic rings in SB1 is about 12.03° with intramolecular O–H \cdots N hydrogen bonds (H \cdots A: 1.85 Å, θ : 146.98°). Crystal face indexing revealed that the two long crystallographic faces of the crystal are (100)/($\bar{1}00$) and (001)/(00 $\bar{1}$), and that its top corresponds to the minor face (010)/(0 $\bar{1}0$) (Figure 1a and Figure S3.1, Supporting Information). The SB1 molecules are slip-stacked via $\pi\cdots\pi$ interactions (3.50 Å) along the growth axis of the crystal (*b*-axis) to construct a columnar assembly. These stacked columns are also close-packed via type II Cl \cdots Cl (3.572 Å, 108.42° , 150.65°) and C–H \cdots O (2.76 Å, 119.31°) interactions in the orthogonal direction, which leads to the formation of slip-planes parallel to the [010] direction in the *bc*-plane. Moreover, the stacked columns are further stabilized by weak dispersive C–H $\cdots\pi$ (2.91 Å) and C–H \cdots Cl (2.95 Å) contacts. Energy framework calculations confirmed that the pairwise interactions between SB1 molecules along the *b*-axis are dominant ($\pi\cdots\pi$ stacking; -50.0 kJ.mol $^{-1}$). In the orthogonal directions to $\pi\cdots\pi$ stacking, the total pairwise interaction energies are ≈ -18.3 kJ.mol $^{-1}$ (C–H \cdots Cl and C–H $\cdots\pi$ interactions) and 36.1 kJ.mol $^{-1}$ (C–H \cdots O and Cl \cdots Cl interactions) along the *c*- and *a*-axis in the *ac* plane, respectively. These data suggest that the crystal packing of SB1 is energetically anisotropic, consistent with plastic bending deformation.

SB2 is isomorphous with SB1, and the details of the structural description are provided in Section S3.2 and Figure S3.2, Supporting Information. SB3 also crystallizes in the monoclinic space group $P2_1/c$ with one molecule in the asymmetric unit. The crystallographic packing of SB3 is nearly identical to SB1 and SB2, with some notable exceptions. Unlike SB1 and SB2, the crystal growth axis of SB3 is along the *a*-axis, along which molecules are slip-stacked via $\pi\cdots\pi$ interactions. In SB3 crystals, the (010)/(0 $\bar{1}0$) and (001)/(00 $\bar{1}$) faces are the major faces, with the minor face being the (100)/($\bar{1}00$) (Figure S3.1, Supporting Information). Moreover, the stacked columns are close-packed to form weak interaction planes, that is, slip planes (blue dotted line in Figure 1) along the [100] direction in the *ac*-plane. Energy framework calculations also suggest that crystal packing of SB3 is energetically anisotropic with strong pairwise interaction energies along the $\pi\cdots\pi$ stacking and weaker interactions in both orthogonal directions. Details of the structural description of SB3 are also given in Section S3.2, Supporting Information.

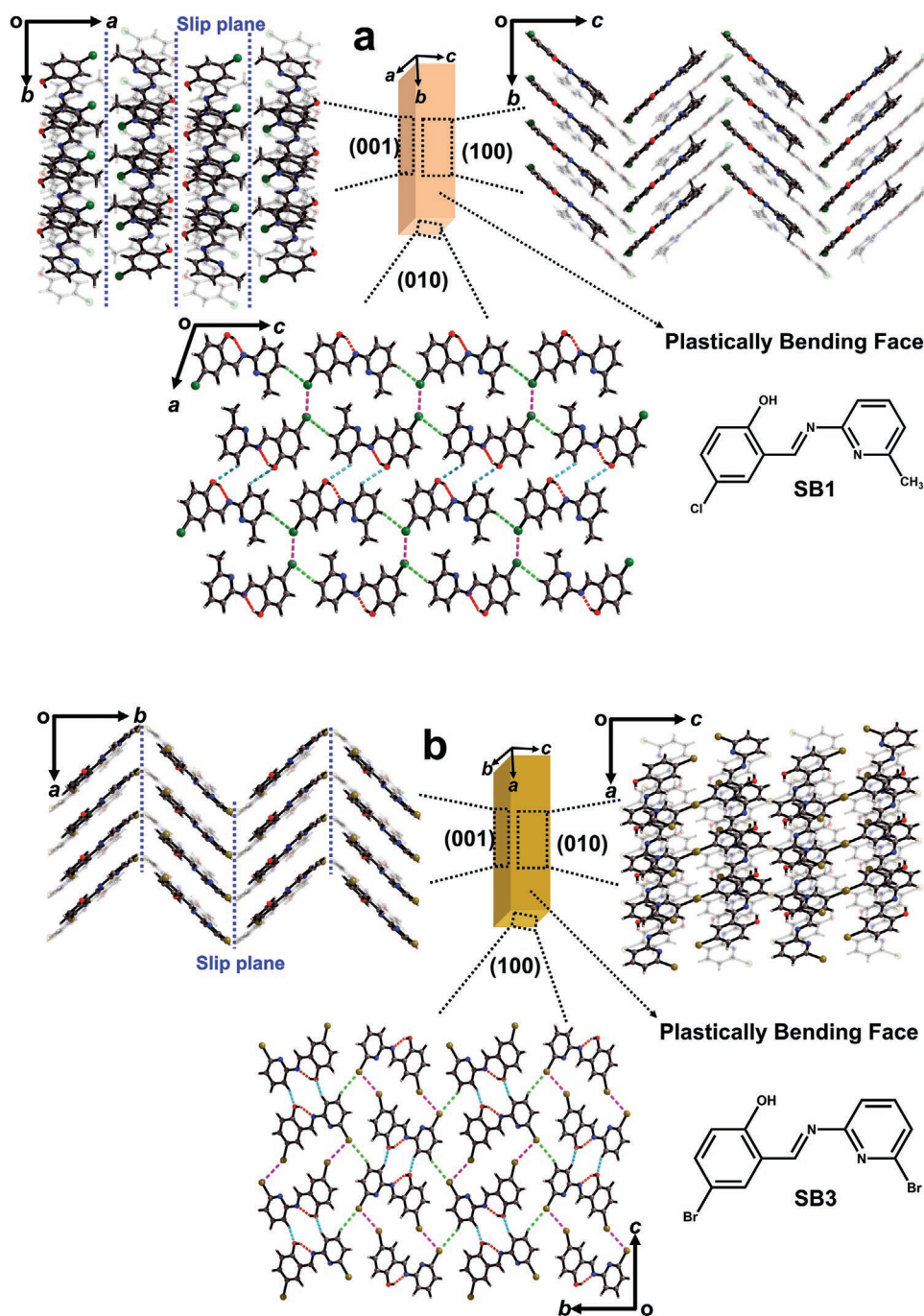


Figure 1. Crystal packing in a) SB1 and b) SB3. View of molecular arrangement on (001), (100), and (010) faces. The blue dotted line presents the slip plane. In the crystal packing molecules are connected to each other via C—H...O (cyan dotted line), type II Cl...Cl and Br...Br (magenta dotted line), C—H...Cl and C—H...Br (green dotted line). The chemical structure of SB1 and SB3 are shown as an inset.

2.2. Crystals Mechanical Properties

The qualitative mechanical properties of macrocrystals of SB1, SB2, and SB3 were examined with the three-point bending method, **Figure 2**. When crystals of SB1 and SB2 were stressed over the (100) face, that is, directly on the slip planes, exceptional and distinct plasticity was observed (Figure 2 i–vi). In contrast, when the crystals were stressed parallel to the herringbone

chains, the crystallographic (001) face, a brittle fracture was observed due to the absence of facile slip planes parallel to this plane. In the case of SB3, applying stress over the (010) face – which corresponds to slip planes parallel to the *ac* plane – caused the crystal to bend without fracture. The (001) face shows brittle fracture upon mechanical stress.

Since all crystals show similar plasticity during three-point bending, the mechanical properties were quantified

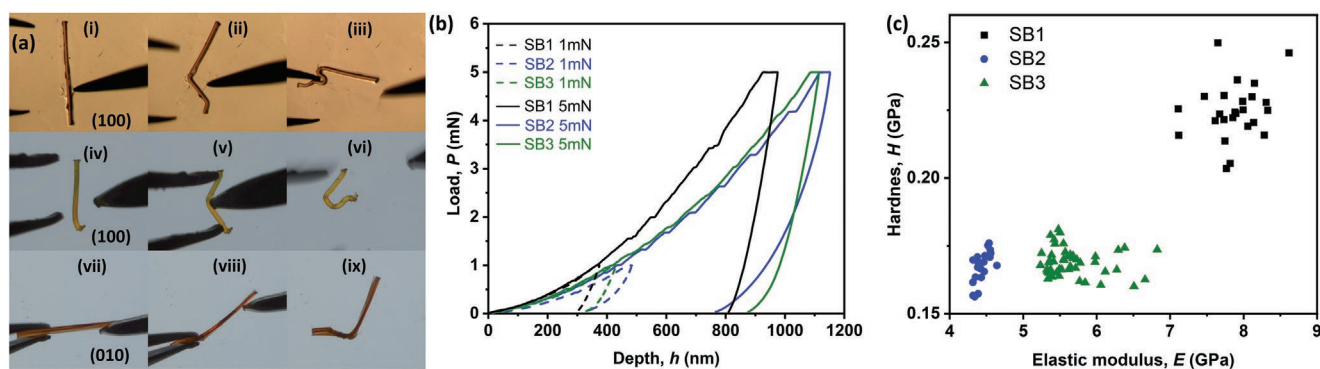


Figure 2. The mechanical properties of plastically flexible crystals. a) Plastic bending nature of SB1 (i–iii), SB2 (iv–vi) and SB3 (vii–ix), respectively, determined by three-point-bending tests; b) representative load–displacement (P – h) curves at 1mN and 5mN loads; c) scatter plot of hardness (H) versus elastic modulus (E) obtained from nanoindentation experiments at a 5 mN load.

by nanoindentation (see Table 1 and Section S6, Supporting Information). The elastic moduli (E , resistance to elastic deformation) and hardness (H , resistance to plastic deformation) were extracted using the standard Oliver–Pharr method^[27] (Table 1). Indentation was performed on the major faces of all the samples [(010) face of crystal SB3 and (100) face of crystals SB1 and SB2, Table 1] with 1 mN and 5 mN peak loads. Representative load–displacement (P – h) curves, the indent impressions left on the crystal faces, and the scatter plot of E and H values are shown in Figure 2. The observed pop-ins or displacement bursts in the P – h curves for all three samples indicate the intermittent plastic deformation, which may be attributed to the presence of slip planes in the structures.^[28] These slip planes are responsible for the plastic deformation on the single crystals’ major faces. Crystal SB1 is the stiffest, with the highest E and H values [8.4 (± 1) GPa and 317 (± 33) MPa, respectively]. The E and H values for all the samples are given in Table 1.

2.3. Optical Properties of SB1 to SB3

Based on salicylaldehyde-derived Schiff bases, the molecules of SB1, SB2, and SB3 were expected to be highly photoluminescent in the solid-state (Figure 3a–c). The SB1, SB2, and SB3 crystals display a broad absorption band with the absorbance tail at ≈ 570 nm. Fluorescence (FL) spectra of SB1 appear in the range of 500–754 nm with two maxima at 551 and 591 nm (Figure 3a). The rod-like crystals of SB2 show a yellow FL (500–775 nm) with maxima at 558 and 592 nm (Figure 3b), while the SB3 crystals exhibit bright green FL with a narrow bandwidth (500–747 nm), showing two maxima at 541 and 579 nm (Figure 3c).

The ≈ 70 nm overlap of SB1 and SB3 FL spectra with the optical absorption of SB3 and SB1, respectively, facilitate the optical energy transfer (ET) from SB1 to SB3 and SB3 to SB1 molecules (Figure 3d). The absolute fluorescence quantum yield of SB1, SB2, and SB3 were measured to be 1.34%, 0.50%, and 0.45%, respectively.

2.4. Micromechanical Flexibility and Photonic Aspects of SB2 Single Crystals

To check the waveguiding properties of SB2 microcrystals, we chose a straight crystal with a length of ≈ 217 μm (Figure 4a–i). The selected crystal was excited with a 405 nm laser at various positions along the crystal body. The generated yellow FL from the excitation point was efficiently transduced to both termini of the crystal, confirming the active optical waveguiding property of the SB2 microcrystal (Figure 4a–ii). The FL spectra display optical modes (due to the constructive interference of FL waves), inferring the FL light confinement ability of the SB2 microcrystals (Figure 4b). Due to the cavity-crystal’s rectangular geometry, the modes could be assigned to Fabry–Pérot (FP) type. The waveguide optical loss coefficient (α) is 0.0855 $\text{dB } \mu\text{m}^{-1}$ (Figure 4c) and was measured by fitting the plot of FL propagation distance (L) versus intensity ratio ($I_{\text{tip}}/I_{\text{body}}$) (where I_{tip} and I_{body} are FL intensities at the spectral collection and excitation position, respectively).

To test the micromechanical flexibility of SB2 single-crystal waveguide-cavity, the straight crystal was mechanically bent into a U-shaped geometry via a mechanophotonics approach (Figure 4d and Figure S71, Supporting Information). The microcrystal was bent in a stepwise manner by aligning the AFM cantilever tip near the left tip of the crystal by

Table 1. Quantitative mechanical properties of SB1, SB2, and SB3 (see Section S6, Supporting Information).

Sample Name	Elastic Modulus (E , GPa)		Hardness (H , MPa)	
	1 mN	5 mN	1 mN	5 mN
SB1 (major face, (100))	8.4 (± 1)	7.87 (± 0.35)	317 (± 33)	224 (± 10)
SB2 (major face, (100))	4.54 (± 0.45)	4.43 (± 0.09)	204 (± 12)	167 (± 5)
SB3 (major face, (010))	7.05 (± 0.25)	5.67 (± 0.38)	214 (± 10)	169 (± 5)

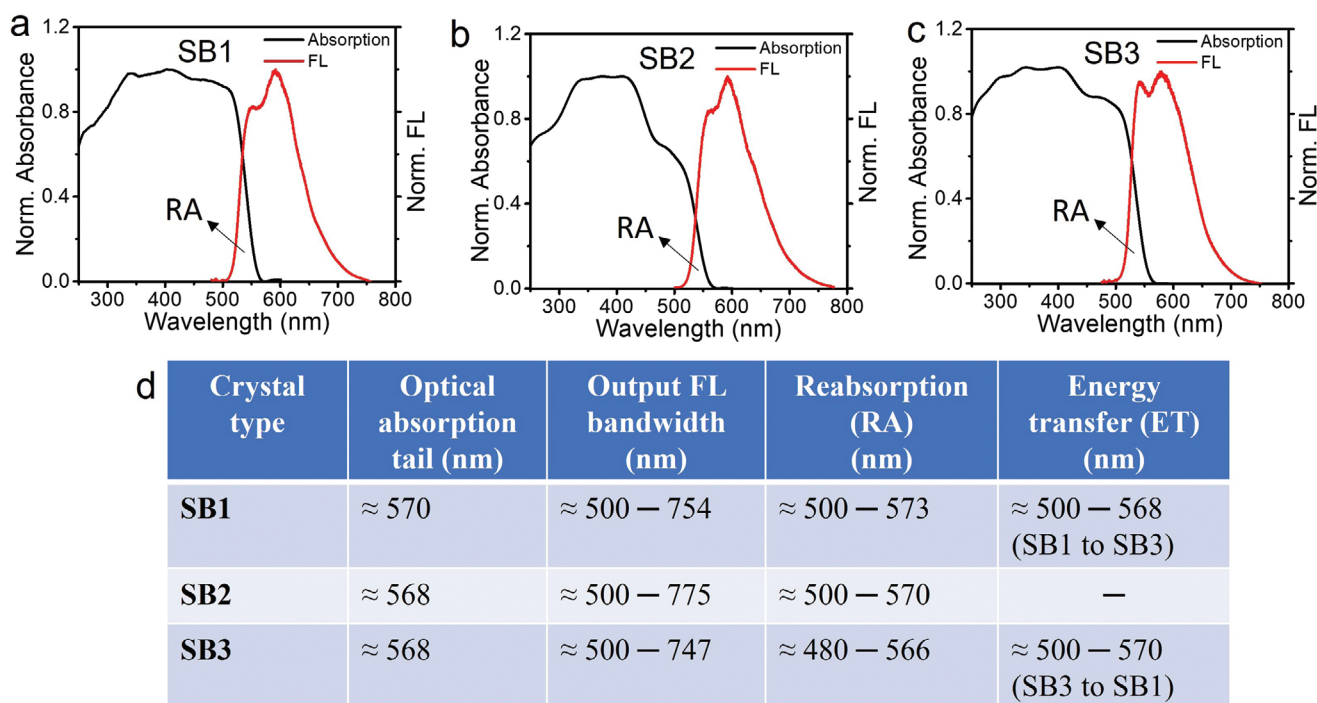


Figure 3. a–c) Solid-state absorbance and fluorescence spectra of SB1, SB2, and SB3. d) Optical properties of SB1, SB2, and SB3 crystals.

moving the stage. A gentle force was applied in the forward direction ($-y$) to bend the crystal to $\approx 90^\circ$ (Figure S7.1i–iii, Supporting Information). The AFM cantilever was then positioned to the right side of the crystal, and force was applied in the $-x$ and $-y$ -directions to create the desired inverted U-shaped geometry with both ends pointing nearly parallel to each other (Figure S7.1iv–viii, Supporting Information). The U-shaped crystal was subjected to laser excitation-position-dependent optical waveguiding studies (Figure 4d-ii). The FL is efficiently transduced to both ends of the crystal even in the bent geometry. The excitation-position-dependent FL spectra also show optical modes, which are different from the straight crystal due to a change of crystal shape (Figure 4e). The α' value of the U-shaped crystal ($0.1103 \text{ dB } \mu\text{m}^{-1}$) was higher than its straight geometry ($0.0855 \text{ dB } \mu\text{m}^{-1}$), which is attributed to the light seepage from the bent region (Figure 4f).

2.5. Construction of Ring-Resonator, and Monolithic OPIC-A/OPIC-B

The construction of a monolithic circuit (OPIC-A) necessitated the fabrication of a ring resonator (RR) from SB3 straight crystal waveguide of length, $L \approx 241 \mu\text{m}$ (OW1) (Figure 5a-i). The optical waveguiding investigations confirmed the FL light transducing tendency of OW1 (Figure 5a-ii–iv and Figure S7.2, Supporting Information). Remarkably, laser light excitation at either of the two ports (P1 or P2) of OW1 displayed optical modes in the FL band (Figure 5b,c). To make a RR, the OW1 waveguide was mechanically bent into an O- or ring-shape by connecting its ends in an edge-to-edge fashion (Figure 5d-i and Figure S7.3, Supporting Information). The horizontal and

vertical diameters of the RR were ≈ 71 and $\approx 61 \mu\text{m}$, respectively (Figure 5d-ii). During the optical excitation of the RR at P1 and P2, the FL propagated either clockwise or counter-clockwise (Figure 5d-iii,iv) as evident from the spectra recorded at the respective output terminals P2 and P1 (Figure 5e,f). The excitation-position-dependent optical waveguiding investigation of the RR shows optical modes in the FL spectra (Figure S7.4, Supporting Information).

To fabricate a monolithic RR coupled waveguide based on an SB3 crystal, an OW2 with length $L \approx 229 \mu\text{m}$ was selected (Figure 6a-i,ii and Figure S7.5, Supporting Information). When either end of the crystal was excited (P3 or P4; Figure 6a-iii,iv) by the laser, an FP mode output signal was measured at the opposite end (Figure 6b,c). For the integration of the RR and OW2, the cantilever tip force was applied along the $-y$ direction, at the left, right, and center of the OW2 crystal, resulting in a monolithic circuit, OPIC-A (Figure 6d-i,ii and Figure S7.6, Supporting Information). OPIC-A was subjected to optical waveguiding experiments by optically exciting at P3 position. The generated green FL transduced to P4 and also passively coupled to the RR at the junction (via evanescent field), taking an anticlockwise path and recombined with the waveguide (Figure 6d-iii). Similar optical behavior was realized when P4 was excited, and the FL routed in a clockwise direction to outcouple at P3 position (Figure 6d-iv). The FL spectra at P4 and P3 positions reveal optical modes (Figure 6e,f), which are different from the uncoupled OW2 waveguide at the same spectral collection points due to optical interference (Figure 6b,c).

To enhance the coupling between the OW2 waveguide-cavity and the RR, the straight OW2 crystal in OPIC-A was bent into an inverted U-shape by applying cantilever tip force at both sides of the crystal, producing an OPIC-B (Figure 6g-i

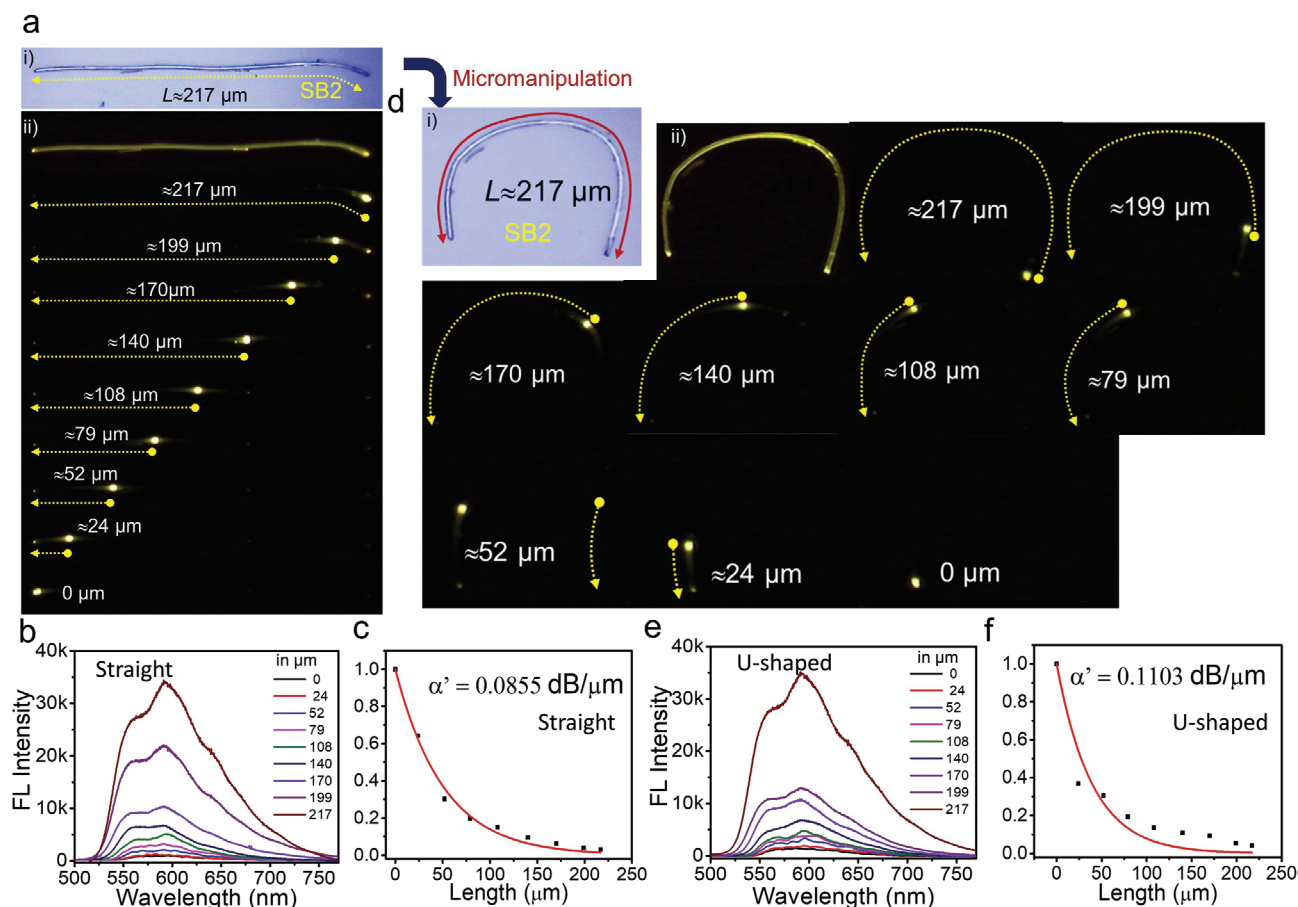


Figure 4. Confocal a-i) optical, and a-ii) FL images of a single straight SB2 crystal of $L \approx 217 \mu\text{m}$ excited with a 405 nm laser at different positions along the crystal. b) The corresponding excitation-position-dependent FL spectra. d-i) Confocal optical and d-ii) FL images of a U-shaped SB2 crystal fabricated by bending the straight crystal via mechanical micromanipulation. The FL images depict excitation along the bent crystal at different positions. e) The corresponding excitation-position-dependent FL spectra. c, f) Estimated optical loss coefficient (α') from the plot of light propagation distance versus $l_{\text{tip}}/l_{\text{body}}$ of the straight and the U-shaped crystals.

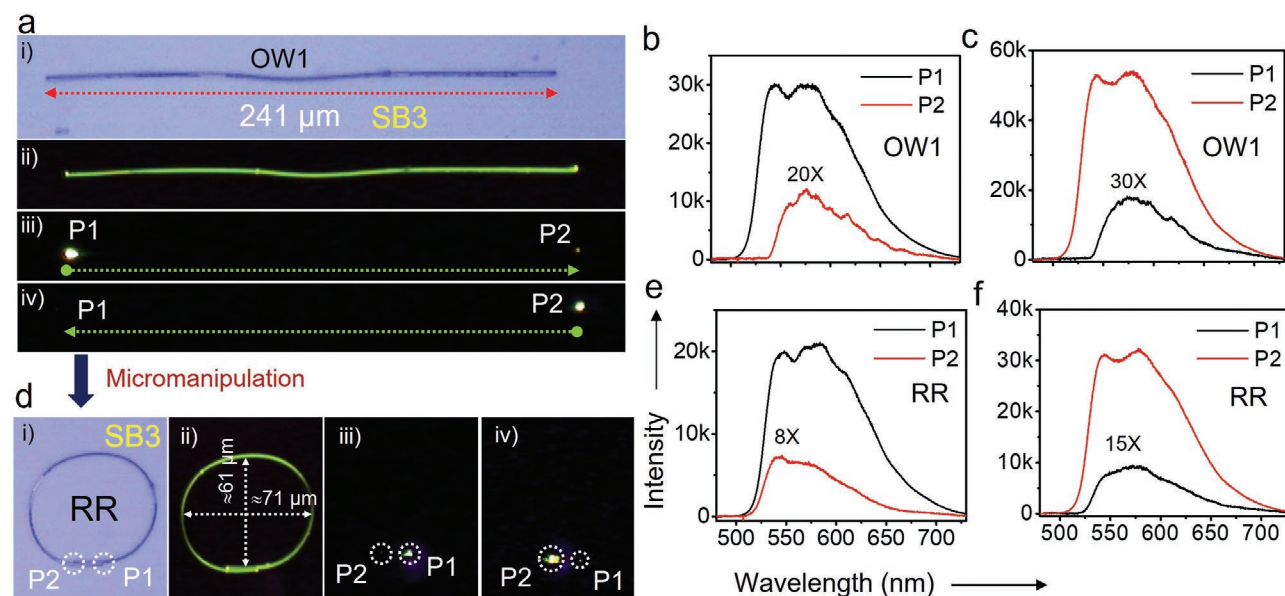


Figure 5. a-i) Confocal optical, and a-ii) FL images of a straight SB3 single-crystal waveguide, OW1. FL images depicting optical excitation of OW1 at a-iii) P1 and a-iv) P2, and the corresponding input and output FL spectra are shown in b, c). d-i) Confocal optical, and d-ii) FL image of RR fabricated from single-crystal SB3. FL images depicting optical excitation of OW1 at d-iii) P1 and d-iv) P2, and the corresponding input and output FL spectra are shown in e, f).

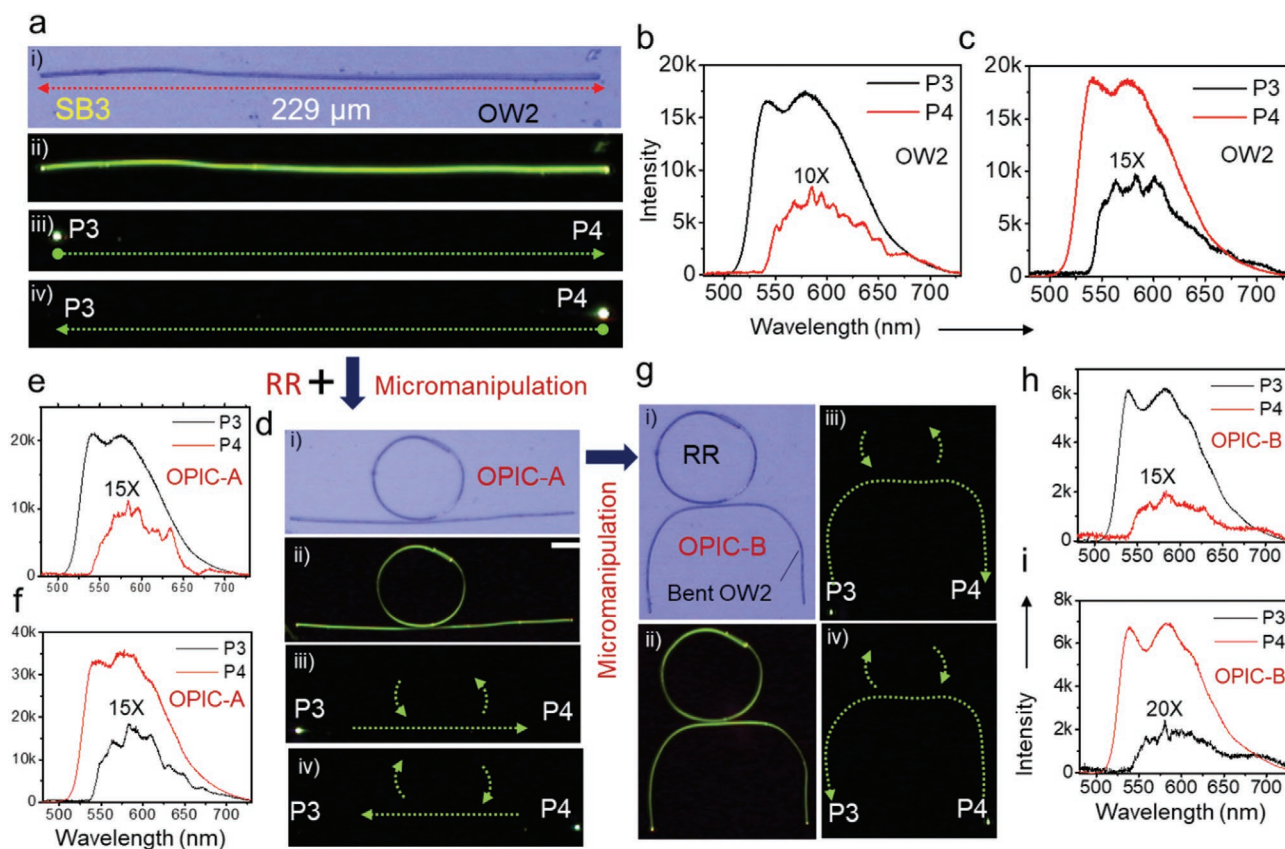


Figure 6. a-i) Confocal optical, and a-ii) FL images of a straight SB3 single-crystal waveguide, OW2. FL images depicting optical excitation of OW2 waveguide at a-iii) P-3, a-iv) P-4, and the corresponding input and output FL spectra are shown in (b) and (c). d-i) Confocal optical and d-ii) FL images of monolithic OPIC-A fabricated from SB3 crystals. FL images depicting optical excitation of OPIC-A at d-iii) P3, d-iv) P4, and the corresponding input and output FL spectra are shown in (e) and (f). g-i) Confocal optical, and g-ii) FL images of monolithic OPIC-B. FL images depicting optical excitation of OPIC-B at g-iii) P3, g-iv) P4, and the corresponding input and output FL spectra are shown in (h) and (i).

and ESI Figure S77, Supporting Information). The convex coupling region was expected to facilitate effective inter-crystal optical coupling (Figure 6g-i,ii). The constructed OPIC-B was

subjected to waveguiding studies by exciting at P3 and P4 and the output signal was recorded at P4 and P3 points, respectively (Figure 6g-iii,iv). Similar to the OPIC-A, the RR routes the

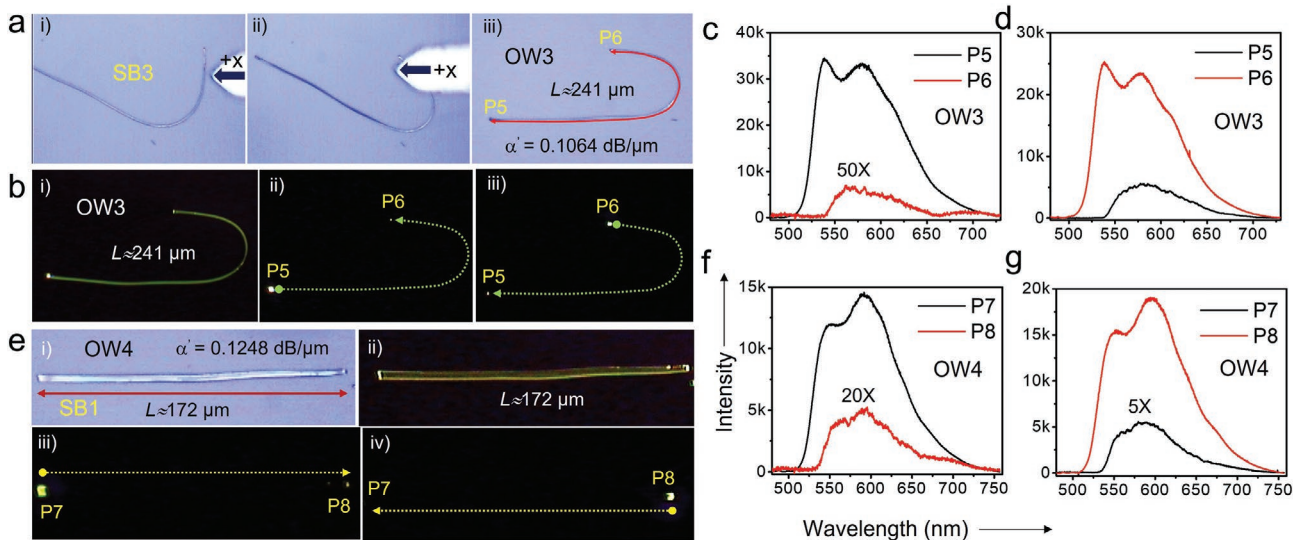


Figure 7. a) Confocal optical images depicting the steps involved in the mechanical micromanipulation of a SB3 single crystal (OW3) into a hook-shape. b-i) FL images of OW3 optically excited at b-ii) P5 and b-iii) P6 termini. The corresponding FL spectra are shown in (c) and (d). e-i) Confocal optical, and e-ii) FL images of a straight OW4 microcrystal of SB1 excited at e-iii) P7 and e-iv) P8 termini. The corresponding FL spectra are shown in (f) and (g).

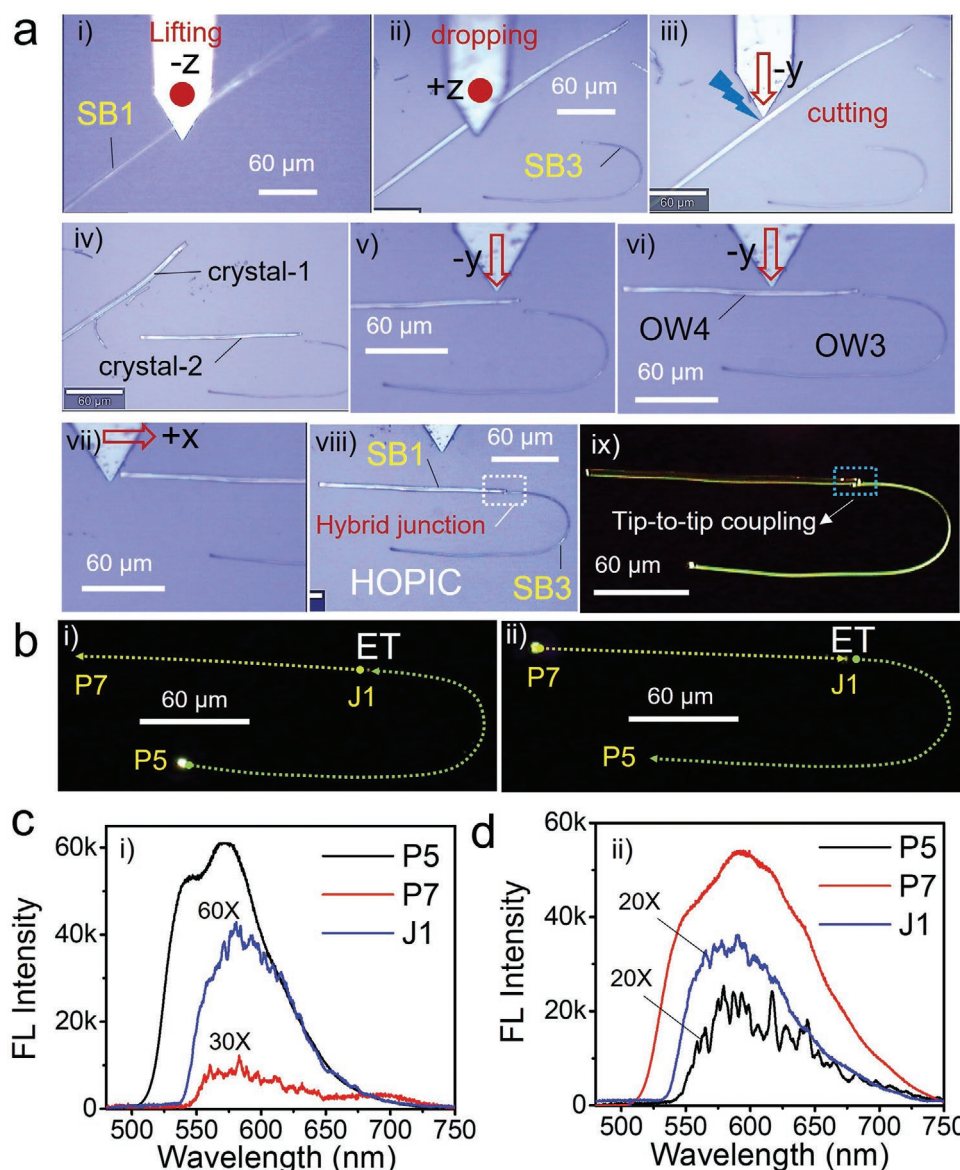


Figure 8. a) Confocal optical images depicting crystal mechanical manipulation steps (lifting, dropping, cutting and integrating) involved in the fabrication of HOPIC using straight SB1 crystal (OW4) and hook-shaped SB3 crystal (OW3). b-i,ii) FL images of HOPIC excited at P5 and P7, respectively. c,d) FL spectra collected at input and outputs ports and the junction, J1.

input signal in a clockwise and counter-clockwise path based on the input excitation terminal. The obtained optical modes at output P3 and P4 (Figure 6h,i) are different from the uncoupled OW2 (Figure 6b,c) and OPIC-A outputs (Figure 6e,f), owing to change of OW2 from straight to bent.

2.6. Fabrication of Hybrid Organic Photonic Integrated Circuit (HOPIC) from OW3 and OW4

For constructing a hybrid OPIC (HOPIC) using SB1 (OW4) and SB3 (OW3) microcrystals, a SB3 crystal waveguide (OW3) of $L \approx 241 \mu\text{m}$ was selected. The selected waveguide was mechanically pushed at the left side of the crystal by applying force in the +x-directions, resulting in a hook-shaped geometry

(Figure 7ai–iii). Initially, the optical transducing behavior of OW3 crystal was tested by exciting at P5 or P6, respectively (Figure 7bi–iii). The corresponding output spectral signals collected at P6 or P5 positions exhibited weak optical modes (Figure 7c,d).

The excitation-position-dependent optical studies showed an increase of FL intensity with the decrease in the optical path length (L) of the waveguide cavity (Figure S7.8a,b, Supporting Information). The OW3 waveguide α is $0.1064 \text{ dB } \mu\text{m}^{-1}$ (Figure S7.8c, Supporting Information). Later, the optical properties of SB1 microcrystal of $L \approx 172 \mu\text{m}$ (OW4) were investigated by exciting at P7 or P8 (Figure 7ei–iv), and the output signal at P8 or P7 shows the optical modes in the FL band (Figure 7f,g). The α of OW4 measured to be $0.1248 \text{ dB } \mu\text{m}^{-1}$ (Figure S7.9a–c, Supporting Information).

Tip-to-tip integration of a straight SB1 crystal (OW4) with a hook-shaped SB3 crystal (OW3) via mechanical micromanipulation is a difficult task. For that, the OW4 crystal was lifted (-z-direction) from substrate-2 with the help of AFM cantilever tip and then transferred onto substrate-1 by cautiously dropping it (+z-direction) close to the OW3 crystal (Figure 8ai,ii). Later, the OW4 crystal was precisely cut into the desired length by applying force in the -y direction (Figure 8aiii,iv). Finally, the hook-shaped OW3 crystal was integrated with OW4 waveguide by pushing the latter in the forward direction (-y-direction) and left tip (+x direction) toward the SB3 crystal, producing a unique tip-to-tip coupled hybrid junction (J1), namely, HOPIC. (Figure 8avi–ix).

To test the optical performance of HOPIC, the P5 of HOPIC was excited with a 405 nm laser, the produced green FL from the excitation point transduces to the junction, J1 (Figure 8b-i). At the hybrid junction, the long-pass filtered (due to reabsorbance) green FL signal optically excited OW4 waveguide tip through an energy transfer mechanism, and the resultant OW4 FL was delivered at P7 (Figure 8b-i). The FL spectra recorded at P7 and J1 exhibited enhanced optical modes compared to those collected for the OW3 waveguide at the same points before circuit fabrication (Figure 8c). Later, the input excitation position moved to P7 position of the HOPIC and output signals were recorded at J1 and P5 (Figure 8bii,d). Interestingly, optical modes at these ports revealed well-separated modes, especially at P5 position, which may be attributed to some of the modes matching in OW4 and OW3, thereby enhancing the optical modes in the FL spectrum.

3. Conclusion

In summary, we prepared three mechanically plastic crystals from Schiff base compounds, abbreviated as SB1, SB2, and SB3. When external stress was applied, the anisotropic molecular packing with slip planes provided permanent deformation to these crystals. SB1 and SB2 crystals bent when stress was applied to the (100) face, whereas SB3 crystals bent over the (010) face, parallel to their slip planes. SB1 and SB3 crystals exhibited FL from ≈ 500 –750 nm, whereas SB2 FL appeared from ≈ 500 –775 nm. Crystals SB1–SB3 reabsorbed their FL in the ≈ 500 –573 nm, ≈ 500 –570 nm and ≈ 480 –566 nm regions, respectively. Notably, the absorbance and emission spectra exhibited energy-transfer possibility from SB1 to SB3, and SB3 to SB1 in the 500–570 nm region. These plastically deformable flexible crystals displayed active optical waveguiding tendency in their straight and 180° (U- and J-shapes) and 360° (O-shaped ring) bent geometries. Using mechanophotonics, a monolithic circuit was fabricated by integrating the convex part of U-shaped and O-shaped SB3 crystals. Later, a hybrid circuit was fabricated by connecting one of the tips of a straight SB1 crystal and a hook-shaped SB3 crystal, facilitating a unique tip-to-tip coupling. The monolithic and hybrid circuits transduced optical signals via active, passive, energy transfer, and reabsorbance mechanisms. Due to the involvement of two electronically different crystals, the hybrid circuit demonstrated light transduction via energy transfer mechanisms.

Supporting Information

Supporting Information is available from the Wiley Online Library or from the author.

Acknowledgements

J.R. and T.F. contributed equally to this work. R.C. thanks the financial support of UoH-IoE [MHRD (F11/9/2019-U3(A); UoH-RC1/RC1-20-003 (F11/9/2019-U3(A); UoH-RC1/RC1-20-003)]. B.B. acknowledges funding from Deutsche Forschungsgemeinschaft, Project No. 450137475. C.M.R. thanks DST-SERB for financial support (CRG/2021/004992).

Open access funding enabled and organized by Projekt DEAL.

Conflict of Interest

The authors declare no conflict of interest.

Data Availability Statement

The data that support the findings of this study are available from the corresponding author upon reasonable request.

Keywords

circuits, mechanophotonics, organic photonics, plastic bendable crystals, waveguides

Received: June 30, 2022
Revised: September 20, 2022
Published online:

- [1] a) R. Chandrasekar, *Chem. Commun.* **2022**, *58*, 3415; b) R. Chandrasekar, *Small* **2021**, *17*, 2100277; c) M. Annadhasan, S. Basak, N. Chandrasekhar, R. Chandrasekar, *Adv. Opt. Mater.* **2020**, *8*, 2000959.
- [2] C. Zhang, C.-L. Zou, Y. Zhao, C.-H. Dong, C. Wei, H. Wang, Y. Liu, G.-C. Guo, J. Yao, Y. S. Zhao, *Sci. Adv.* **2015**, *1*, 1:e1500257.
- [3] L. Coldren, S. Corzine, M. Mashanovitch, *Diode Lasers and Photonic Integrated Circuits*, 2nd ed., Wiley, Hoboken, NJ, **2012**.
- [4] a) W. Bogaerts, L. Chrostowski, *Laser Photonics Rev.* **2018**, *12*, 1700237; b) D. Thomson, A. Zilkie, J. E. Bowers, T. Komljenovic, G. T. Reed, L. Vivien, D. Marris-Morini, E. Cassan, L. Viro, J.-M. Fédéli, J.-M. Hartmann, J. H. Schmid, D.-X. Xu, F. Boeuf, P. O'Brien, G. Z. Mashanovich, M. Nedeljkovic, *J. Opt.* **2016**, *18*, 073003; c) W. Bogaerts, D. Pérez, J. Capmany, D. A. B. Miller, J. Poon, D. Englund, F. Morichetti, A. Melloni, *Nature* **2020**, *586*, 207.
- [5] H. S. Rong, Y. H. Kuo, A. S. Liu, M. Paniccia, O. Cohen, *Opt. Express* **2006**, *14*, 1182.
- [6] W. Bogaerts, R. Baets, P. Dumon, V. Wiaux, S. Beckx, D. Taillaert, B. Luyssaert, J. V. Campenhout, P. Bienstman, D. V. Thourhout, *J. Lightwave Technol.* **2005**, *23*, 401.
- [7] a) K. Takazawa, J.-i. Inoue, K. Mitsuishi, T. Takamasu, *Phys. Rev. Lett.* **2010**, *105*, 067401; b) Z. Jiang, A. Ren, Y. Yan, J. Yao, Y. S. Zhao, *Adv. Mater.* **2022**, *34*, 2106095.
- [8] Z. Yu, Y. Wu, L. Xiao, J. Chen, Q. Liao, J. Yao, H. Fu, *J. Am. Chem. Soc.* **2017**, *139*, 6376.

- [9] K. Takazawa, Y. Kitahama, Y. Kimura, G. Kido, *Nano Lett.* **2005**, *5*, 1293.
- [10] a) N. Chandrasekar, M. A. Mohiddon, R. Chandrasekar, *Adv. Opt. Mater.* **2013**, *1*, 305; b) N. Chandrasekar, R. Chandrasekar, *Angew. Chem., Int. Ed.* **2012**, *51*, 3556.
- [11] a) J. Ravi, D. Venkatakrishnarao, C. Sahoo, S. R. G. Naraharisetty, N. Mitetelo, A. A. Ezhov, E. Mamonov, T. Murzina, R. Chandrasekar, *ChemNanoMat* **2018**, *4*, 764; b) N. Mitetelo, D. Venkatakrishnarao, J. Ravi, M. Popov, E. Mamonov, T. V. Murzina, R. Chandrasekar, *Adv. Opt. Mater.* **2019**, *7*, 1801775; c) V. V. Pradeep, N. Mitetelo, M. Annadhasan, M. Popov, E. Mamonov, T. Murzina, R. Chandrasekar, *Adv. Opt. Mater.* **2020**, *8*, 1901317; d) V. Radhika, M. Annadhasan, J. Ravi, M. D. Durga Prasad, N. Mitetelo, K. Zhdanova, E. Mamonov, K. Muellen, T. V. Murzina, R. Chandrasekar, *Adv. Opt. Mater.* **2020**, *8*, 2000431.
- [12] a) D. Venkatakrishnarao, C. Sahoo, E. A. Mamonov, V. B. Novikov, N. V. Mitetelo, S. R. G. Naraharisetty, T. V. Murzina, R. Chandrasekar, *J. Mater. Chem. C* **2017**, *5*, 12349.
- [13] a) C. M. Reddy, R. C. Gundakaram, S. Basavoju, M. T. Kirchner, K. A. Padmanabhan, G. R. Desiraju, *Chem. Commun.* **2005**, *31*, 3945; b) C. M. Reddy, G. R. Krishna, S. Ghosh, *CrystEngComm.* **2010**, *12*, 2296; c) M. K. Panda, S. Ghosh, N. Yasuda, T. Moriwaki, G. D. Mukherjee, C. M. Reddy, P. Naumov, *Nat. Chem.* **2015**, *7*, 65; d) G. R. Krishna, R. Devarapalli, G. Lal, C. M. Reddy, *J. Am. Chem. Soc.* **2016**, *138*, 13561; e) S. Saha, M. K. Mishra, C. M. Reddy, G. R. Desiraju, *Acc. Chem. Res.* **2018**, *51*, 2957; f) A. Mondal, B. Bhattacharya, S. Das, S. Bhunia, R. Chowdhury, S. Dey, C. M. Reddy, *Angew. Chem., Int. Ed.* **2020**, *59*, 10971.
- [14] a) S. Ghosh, C. M. Reddy, *Angew. Chem., Int. Ed.* **2012**, *51*, 10319; b) H. Liu, K. Ye, Z. Zhang, H. Zhang, *Angew. Chem., Int. Ed.* **2019**, *58*, 19081; c) X. Pan, A. Zheng, X. Yu, Q. Di, L. Li, P. Duan, K. Ye, P. Naumov, H. Zhang, *Angew. Chem., Int. Ed.* **2022**, *61*, e202203938.
- [15] a) P. Naumov, S. Chizhik, M. K. Panda, N. K. Nath, E. Boldyreva, *Chem. Rev.* **2015**, *115*, 12440; b) S. Das, A. Mondal, C. M. Reddy, *Chem. Soc. Rev.* **2020**, *49*, 8878; c) E. Ahmed, D. P. Karothu, P. Naumov, *Angew. Chem., Int. Ed.* **2018**, *57*, 8837; d) S. Hayashi, T. Koizumi, *Angew. Chem., Int. Ed.* **2016**, *55*, 2701; e) H. Liu, Z. Lu, Z. Zhang, Y. Wang, H. Zhang, *Angew. Chem., Int. Ed.* **2018**, *57*, 8448; f) M. Rohullah, V. V. Pradeep, J. Ravi, A. V. Kumar, R. Chandrasekar, *Angew. Chem., Int. Ed.* **2022**, *61*, e202202114.
- [16] a) R. Chandrasekar, *Phys. Chem. Chem. Phys.* **2014**, *16*, 7173; b) P. Hui, R. Chandrasekar, *Adv. Mater.* **2013**, *25*, 2963; c) U. Venkataramudu, D. Venkatakrishnarao, N. Chandrasekar, M. A. Mohiddon, R. Chandrasekar, *Phys. Chem. Chem. Phys.* **2016**, *18*, 15528; d) D. Venkatakrishnarao, M. A. Mohiddon, N. Chandrasekar, R. Chandrasekar, *Adv. Opt. Mater.* **2015**, *3*, 1035; e) S. Basak, R. Chandrasekar, *J. Mater. Chem. C* **2014**, *2*, 1404.
- [17] a) Q. Kong, Q. Liao, Z. Xu, X. Wang, J. Yao, H. Fu, *J. Am. Chem. Soc.* **2014**, *136*, 2382; b) H. Liu, Z. Lu, B. Tang, C. Qu, Z. Zhang, H. Zhang, *Angew. Chem., Int. Ed.* **2020**, *59*, 12944; c) S. Chen, M.-P. Zhuo, X.-D. Wang, G.-Q. Wei, L.-S. Liao, *Photonix.* **2021**, *2*, 2; d) M. Annadhasan, D. P. Karothu, R. Chinnasamy, L. Catalano, E. Ahmed, S. Ghosh, P. Naumov, R. Chandrasekar, *Angew. Chem., Int. Ed.* **2020**, *59*, 13821; e) S. Zhao, H. Yamagishi, O. Oki, Y. Ihara, N. Ichiji, A. Kubo, S. Hayashi, Y. Yamamoto, *Adv. Opt. Mater.* **2022**, *10*, 2101808.
- [18] K. Takazawa, J.-i. Inoue, K. Mitsuishi, T. Kuroda, *Adv. Funct. Mater.* **2013**, *23*, 839.
- [19] J. Ravi, R. Chandrasekar, *Adv. Opt. Mater.* **2021**, *9*, 2100550.
- [20] a) D. Venkatakrishnarao, R. Chandrasekar, *Adv. Opt. Mater.* **2016**, *4*, 112; b) M. Annadhasan, U. Venkataramudu, N. V. Mitetelo, E. A. Mamonov, C. Sahoo, S. R. G. Naraharisetty, T. V. Murzina, R. Chandrasekar, *ACS Appl. Energy Mater.* **2019**, *2*, 428.
- [21] a) Y. C. Tao, X. D. Wang, L. S. Liao, *J. Mater. Chem. C* **2019**, *7*, 3443; b) S. Kushida, D. Braam, C. Pan, T. D. Dao, K. Tabata, K. Sugiyasu, M. Takeuchi, S. Ishii, T. Nagao, A. Lorke, Y. Yamamoto, *Macromolecules* **2015**, *48*, 3928; c) K. Tabata, D. Braam, S. Kushida, L. Tong, J. Kuwabara, T. Kanbara, A. Beckel, A. Lorke, Y. Yamamoto, *Sci. Rep.* **2014**, *4*, 5902.
- [22] a) M. Annadhasan, A. R. Agrawal, S. Bhunia, V. V. Pradeep, S. S. Zade, C. M. Reddy, R. Chandrasekar, *Angew. Chem., Int. Ed.* **2020**, *59*, 13852; b) M. Annadhasan, V. V. Pradeep, A. V. Kumar, J. Ravi, R. Chandrasekar, *Small Struct.* **2022**, *3*, 2100163.
- [23] a) Y. S. Zhao, A. Peng, H. Fu, Y. Ma, J. Yao, *Adv. Mater.* **2008**, *20*, 1661. b) W. Zhang, J. Yao, Y. S. Zhao, *Acc. Chem. Res.* **2016**, *49*, 1691. c) C. Zhang, H. Dong, C. Zhang, Y. Fan, J. Yao, Y. S. Zhao, *Sci. Adv.* **2021**, *7*, eabh3530.
- [24] a) R. Krishna, M. S. R. N. Kiran, C. L. Fraser, U. Ramamurty, C. M. Reddy, *Adv. Funct. Mater.* **2013**, *23*, 1422; b) Z. Lu, Y. Zhang, H. Liu, K. Ye, W. Liu, H. Zhang, *Angew. Chem., Int. Ed.* **2020**, *59*, 4299; c) S. Hayashi, S.-y. Yamamoto, D. Takeuchi, Y. Ie, K. Takagi, *Angew. Chem., Int. Ed.* **2018**, *57*, 17002; d) L. Catalano, D. P. Karothu, S. Schramm, E. Ahmed, R. Rezgui, T. J. Barber, A. Famulari, P. Naumov, *Angew. Chem., Int. Ed.* **2018**, *57*, 17254.
- [25] a) J. Ravi, A. V. Kumar, D. P. Karothu, M. Annadhasan, P. Naumov, R. Chandrasekar, *Adv. Funct. Mater.* **2021**, *31*, 2105415. b) J. Ravi, M. Annadhasan, A. V. Kumar, R. Chandrasekar, *Adv. Funct. Mater.* **2021**, *31*, 2100642; c) A. V. Kumar, R. Chandrasekar, *Adv. Opt. Mater.* **2022**, <https://doi.org/10.1002/adom.202201009>.
- [26] a) T. Feiler, B. Bhattacharya, A. A. L. Michalchuk, S.-Y. Rhim, V. Schröder, E. List-Kratochvil, F. Emmerling, *CrystEngComm* **2021**, *23*, 5815; b) R. Chinnasamy, J. Ravi, V. V. Pradeep, D. Manoharan, F. Emmerling, B. Bhattacharya, S. Ghosh, R. Chandrasekar, *Chemistry - Eur. J.* **2022**, *28*, e202200905.
- [27] a) W. C. Oliver, G. M. Pharr, *J. Mater. Res.* **1992**, *7*, 1564; b) W. C. Oliver, G. M. Pharr, *J. Mater. Res.* **2004**, *19*, 3.
- [28] B. Bhattacharya, D. Roy, S. Dey, A. Puthuvakkal, S. Bhunia, S. Mondal, R. Chowdhury, M. Bhattacharya, M. Mandal, K. Manoj, P. K. Mandal, C. M. Reddy, *Angew. Chem., Int. Ed.* **2020**, *59*, 19878.